Progress In Electromagnetics Research B, Vol. 88, 19–34, 2020

Enhancements of Applications Entailing Higher-Order Floquet Harmonics of Penetrable Metallic Gratings with Bars Loaded with Conducting Fins and Stratified Dielectric Covers on Both Sides

Malcolm Ng Mou Kehn[1, 2, *]

Abstract—There has been a presented modal approach for analyzing the scattering of plane waves that are incident on penetrable gratings with metallic fins lined over both exterior surfaces of each conducting bar to create flanged apertures, which altogether is covered on both sides by multiple dielectric layers. The new degrees of freedom afforded by the special complex geometry offer ways to improve the capabilities of various applications such as beam deflectors, resolution of spectroscopic gratings, grating couplers, and grating pulse compression/decompression, as shall be demonstrated herein for the latter two. All of these entail higher-order diffraction modes, which are advantageously studied by the aforementioned analytical tool. Outcomes of measurements on a fabricated prototype that agree well with expectations from theory are also presented.

1. INTRODUCTION

A full-wave modal technique has been presented in [1] for studying the plane-wave scattering by penetrable metallic gratings whose bars are loaded on both sides by conducting strips, altogether of which are sandwiched by stratified dielectric slabs on both sides. This structure is illustrated by the diagram in Fig. 1. Through the new structural and material attributes offered by the present special geometry, such as those afforded by dielectric slab covers loadable on both sides of the gratings, dielectric filling of the grooves, as well as flanged slits creatable by metallic fins loaded on the conducting bars, the performances of a multitude of applications can be elevated, such as grating couplers [2–4], spectroscopy [5–7], pulse compression and decompression gratings [8–13], grid polarizers [14–16], holography, and polarimetry, among many others in the fields of optics and antennas.

Using the aforementioned analytical tool of [1] for the design process, targeting specifically at higher-ordered Floquet harmonics, how the newly afforded degrees of parametric freedom are able to enhance three showcased examples of applications that make use of these higher diffraction orders are presented in Section 2. Specifically, they are 1) grating couplers, 2) pulse compression and decompression gratings, and 3) resolution of gratings for spectroscopy. The theory behind grating couplers in connection with the modal surface-wave dispersion diagram are described in Section 2.1, making use of clear schematics containing the various wavenumber vectors that altogether portray the underlying mechanisms. The pivotal concept of surface-wave resonance coupling shall then be affirmed by computed results (from codes based on the modal formulation of [1]) for a specific case of grating coupler, via both the dispersion diagram as well as the spectrum of powers carried by the higher diffraction order of interest. How the new parameters provided by the special grating topology are able to boost the power channeled into that latter Floquet mode as well as to maximize the frequency bandwidth over which that is achieved are

Received 20 July 2020, Accepted 30 July 2020, Scheduled 14 August 2020
* Corresponding author: Malcolm Ng Mou Kehn (malcolm.ng@ieee.org).
[1] Institute of Communications Engineering, College of Electrical and Computer Engineering, National Chiao Tung University, Taiwan.
[2] Center for mmWave Smart Radar Systems and Technologies, National Chiao Tung University, Taiwan.

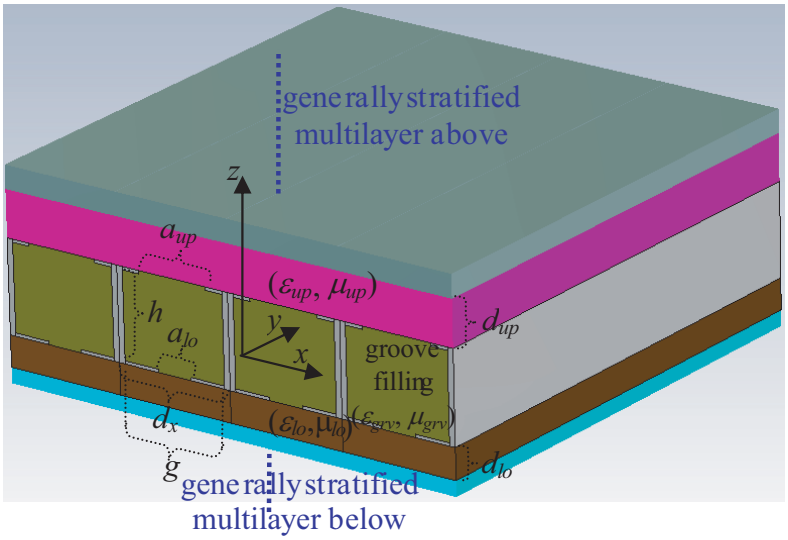

Figure 1. Corrugations with period d_x along x, depth h along z, generally dielectric filled grooves $(\varepsilon_{grv},\ \mu_{grv})$, thin fin strip lined over both upper and lower ends of each ridge (bar) to create flanged groove apertures of widths a_{up} and $a_{\ell o}$, and generally sheathed by multiple layers of dielectric slabs on both sides that sandwich the gratings.

also investigated. In a similar illustrative manner, the concepts behind gratings for pulse compression and decompression are explained in Section 2.2 via a schematic of the physical grating itself that is annotated with ray paths of dispersed diffraction orders and their associated wave-vectors, plus the use of a so-called Floquet lattice diagram. Ways into which the bandwidth and scan-width of the -1 diffraction order may be enhanced by tailoring the newly afforded parameters of the unusual geometry will also be presented. In the final showcased application, improvements in resolutions of diffraction gratings used in spectroscopy are demonstrated by making use of optimized dielectric slab covers, being just among the numerous other parametric degrees of freedom that can provide beneficial effects which are singled out for presentation in this paper. Measurement results from experiments conducted on a manufactured prototype grating shall then be presented in Section 3 followed by sensitivity analyses of manufacture tolerances given in Section 4 using the computational approach of [1]. Conclusions are then drawn in the final section.

2. ENHANCEMENTS OF APPLICATIONS ENTAILING HIGHER-ORDER FLOQUET MODES

The premeditated control of transmitted higher diffraction orders through penetrable gratings in terms of both their propagation directions and intensities constitutes an important subject of study, especially in the context of applications such as beam deflectors, mode converters, as well as diffraction gratings for spectroscopy and pulse compression or stretching. The $m = \pm 1$ diffraction orders are the ones that are most often manipulated and tailored for these aforesaid applications. Capitalizing on the special geometry studied in [1] and depicted by Fig. 1, the upcoming subsections explore the prospects of enhancing the performance of higher-order Floquet harmonics.

2.1. Grating Couplers

Grating couplers are penetrable (ungrounded) diffraction gratings clad on one side with an interfacing dielectric layer such that incident plane waves arriving from the uncovered side get coupled resonantly to a fast-wave slab-mode pertaining to a designated diffraction order. This mechanism offers applications as mode couplers, surface-wave launchers for metasurface (plasmonic) lenses, excitation sources for thin-film waveguides, among others.

Supposing that the $m = 1$ harmonic is the intended one for coupling into a slab mode and $\phi_{inc} = 0$ such that the plane of incidence is perpendicular to the gratings, then Fig. 2 provides a schematic of the mechanism that is to be described as follow. For a certain layer-coated grating topology that produces the surface-wave dispersion diagram such as Fig. 3 computed by the modal method of [1] and validated with commercial software, with a period of d_x, then say, at a given design frequency, f_{des}, with associated prescribed $k_{0des} = 2\pi f_{des}\sqrt{(\mu_0\varepsilon_0)}$, the surface-wave dispersion diagram of the likes of Fig. 3 dictates a particular eigen-modal resonant surface-wave number, say $k_{surf,des}$ ($> k_{0des}$) at that f_{des}. This known $k_{surf,des}$ is then enforced to be equal to the corresponding $m = 1$ Floquet modal wavenumber: $k_{x1des} = k_{0des}\sin\theta_{0des} + 2\pi/d_x$, with θ_{0des} being the unknown incidence angle to be determined, i.e.,

$$k_{0des}\sin\theta_{0des} + 2\pi/d_x = k_{surf,des} \Rightarrow \theta_{0des} = \sin^{-1}\{[k_{surf,des} - (2\pi/d_x)]/k_{0des}\} \tag{1}$$

thereby yielding the angular direction of the incident wave which arrives from the exterior free space that would result in resonant coupling of the energy carried by the incident field to that of the mode within the dielectric slab associated with the $m = 1$ diffraction order. This Eq. (1) means that, at any desired point (f_{des}, $k_{surf,des}$) along a modal dispersion trace of Fig. 3, there corresponds a certain angular direction θ_{0des} of an incident plane wave that would produce resonant coupling of this incident wave to the bounded fast-wave slab-mode. This highlights yet another aspect in which such surface-wave modal dispersion diagrams come in useful. Results that showcase the validity of this above Eq. (1)

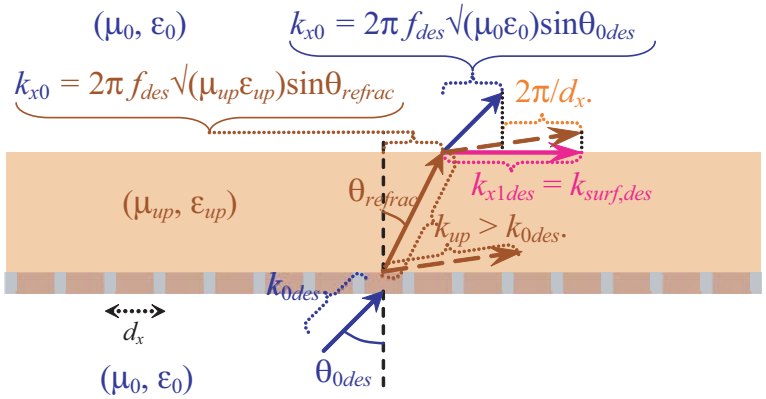

Figure 2. Schematic and mechanism of the grating coupler. The $k_{surf,des}$, which is from the surface-wave dispersion diagram, is equated to k_{x1des} as shown. The two indicated k_{x0} components are equated to each other.

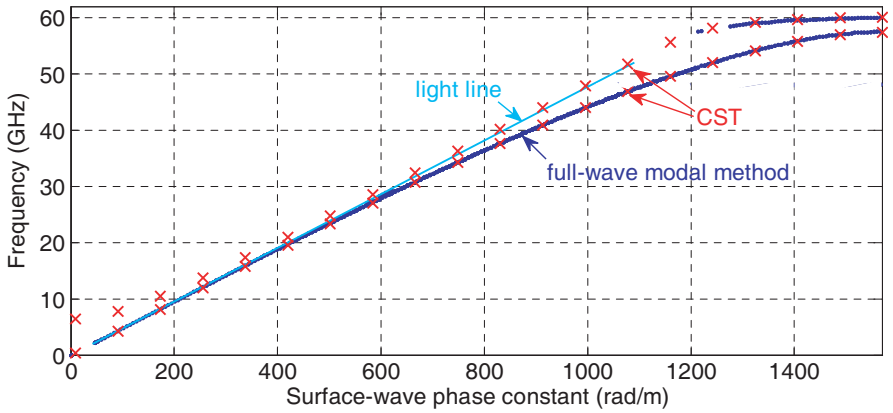

Figure 3. Validation with CST of modal method in [1] in terms of surface-wave dispersion diagram with $\phi_0 = k_{y0} = 0$ (propagation along x), for $d_x = 2\,\text{mm}$, $\varepsilon_{grv}/\varepsilon_0 = 3$, $h = 1\,\text{mm}$, $g = a_{up} = a_{\ell o} = 1.8\,\text{mm}$, $\varepsilon_{\ell o}/\varepsilon_0 = \varepsilon_{up}/\varepsilon_0 = 1.0$ (uncovered on both sides).

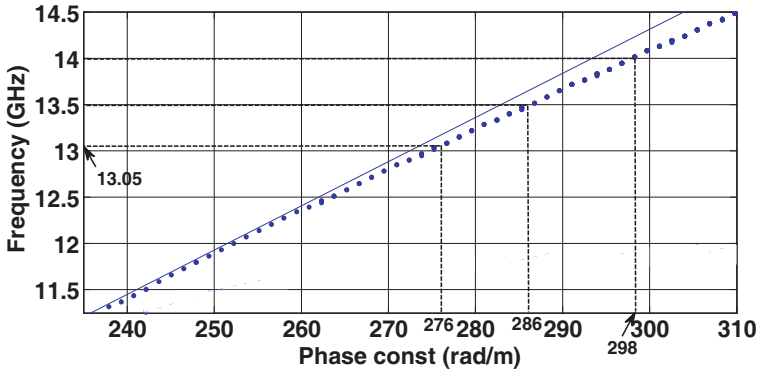

Figure 4. Surface-wave dispersion diagram with $\phi_0 = k_{y0} = 0$ (propagation along x), for $d_x = 20\,\text{mm}$, $\varepsilon_{grv}/\varepsilon_0 = 1$, $h = 12\,\text{mm}$, $g = a_{up} = a_{\ell o} = 14\,\text{mm}$, $\varepsilon_{\ell o}/\varepsilon_0 = 1$, $d_{\ell o} = 1\,\text{mm}$, $\varepsilon_{up}/\varepsilon_0 = 3.38$, $d_{up} = 1.524\,\text{mm}$.

Table 1. Incidence angles for resonant coupling by (53) leftmost two columns from dispersion diagram of Fig. 12.

f_{des} (GHz)	$k_{surf,des}$ (rad/m)	θ_{0des} (degree)
13.05	276	−8.020
13.5	286	−5.712
14	298	−3.157
14.5	310	−0.7842

have been exhaustively computed but are not included due to space constraints.

Figure 4 presents the surface-wave dispersion diagram with $\phi_0 = k_{y0} = 0$ (propagation along x), for a certain grating coupler with the following parameters: $d_x = 20\,\text{mm}$, $\varepsilon_{grv}/\varepsilon_0 = 1$, $h = 12\,\text{mm}$, $g = a_{up} = a_{\ell o} = 14\,\text{mm}$, $\varepsilon_{\ell o}/\varepsilon_0 = 1$, $d_{\ell o} = 1\,\text{mm}$, $\varepsilon_{up}/\varepsilon_0 = 3.38$, $d_{up} = 1.524\,\text{mm}$. For four design frequencies: $f_{des} = 13.05\,\text{GHz}$, $13.5\,\text{GHz}$, $14.0\,\text{GHz}$, and $14.5\,\text{GHz}$, the corresponding $k_{surf,des} = 276\,\text{rad/m}$, $286\,\text{rad/m}$, $298\,\text{rad/m}$, and $310\,\text{rad/m}$ are read off from this graph. The associated θ_{0des} for these four resonant coordinates may then be obtained from Eq. (1), as tabulated in Table 1.

For these four θ_{0des} angles of TM^z polarized plane wave incidence (with $\phi_{inc} = 0$) on this grating coupler, the normalized power carried by the $m = 1$ Floquet harmonic fast-space wave of the bounded slab-mode within the dielectric layer just above the gratings is plotted against frequency in Fig. 5.

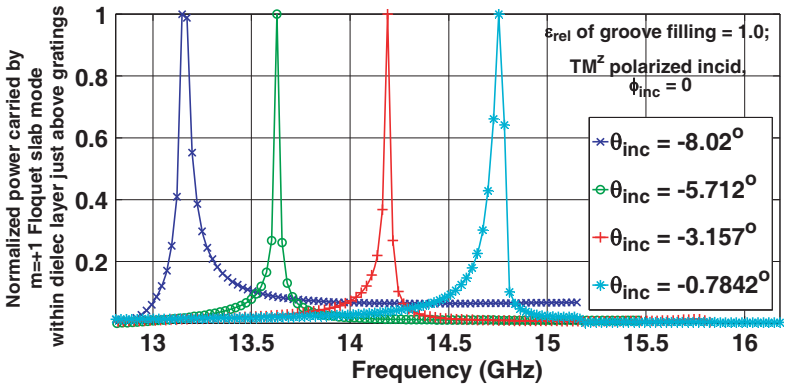

Figure 5. Plot of normalized power carried by $m = +1$ Floquet harmonic fast-space wave of bounded slab-mode within dielectric layer just above gratings against frequency, for $d_x = 20\,\text{mm}$, $\varepsilon_{grv}/\varepsilon_0 = 1$, $h = 12\,\text{mm}$, $g = a_{up} = a_{\ell o} = 14\,\text{mm}$, $\varepsilon_{\ell o}/\varepsilon_0 = 1$, $d_{\ell o} = 1\,\text{mm}$, $\varepsilon_{up}/\varepsilon_0 = 3.38$, $d_{up} = 1.524\,\text{mm}$; for various $\theta_{0des} = \theta_{inc}$ angles (as annotated) of TM^z polarized plane-wave incidence with $\phi_{inc} = 0$.

Indeed, peaks are observed at frequencies (13.15 GHz, 13.6 GHz, 14.17 GHz, and 14.75 GHz) that are close to the respective designed ones: f_{des} and which are also spaced about 0.5 GHz apart. This affirms the underlying mechanism of surface-wave resonance coupling.

We shall now investigate the ways into which the power transferred to the $m = 1$ diffraction order within the dielectric cladding as well as its bandwidth may be maximized by the special topology that is herein studied. To save manuscript space, results for just TM^z polarized plane-wave incidence with $\phi_{inc} = 0$ and $\theta_{inc} = 30^\circ$ are presented.

2.1.1. Groove Permittivity

Optimization by tailoring the permittivity of the groove filling is first studied. Fig. 6 displays the contour plots of the normalized power carried by the $m = 1$ Floquet harmonic fast-space wave of the bounded slab-mode within the dielectric layer just above the gratings against $\varepsilon_{grv}/\varepsilon_0$ and frequency, for $d_x = 20\,\text{mm}$, $g = a_{\ell o} = a_{up} = 14\,\text{mm}$, $h = 12\,\text{mm}$, $\varepsilon_{\ell o}/\varepsilon_0 = 1$, $\varepsilon_{up}/\varepsilon_0 = 10.2$, and $d_{up} = 1.27\,\text{mm}$. Optimal bandwidth is achieved with $\varepsilon_{grv}/\varepsilon_0 \approx 6.3$. This demonstrates the benefits of filling up the grooves with dielectric rather than leaving them conventionally empty.

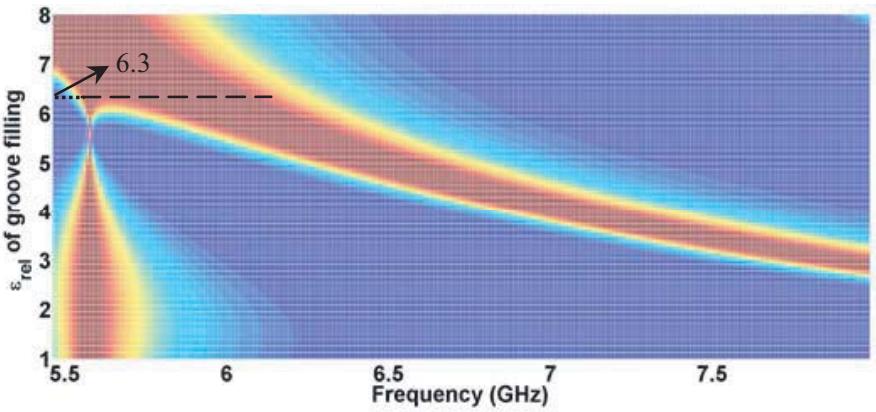

Figure 6. Contour plot of normalized power carried by $m = +1$ Floquet harmonic fast-space wave of bounded slab-mode within dielectric layer just above gratings against frequency and $\varepsilon_{grv}/\varepsilon_0$, for TM^z polarized incidence with $\phi_{inc} = 0$ and $\theta_{inc} = 30^\circ$, with $d_x = 20\,\text{mm}$, $h = 12\,\text{mm}$, $g = a_{\ell o} = a_{up} = 14\,\text{mm}$, $\varepsilon_{\ell o}/\varepsilon_0 = 1$, $\varepsilon_{up}/\varepsilon_0 = 10.2$, $d_{up} = 1.27\,\text{mm}$.

2.1.2. Fins to Create Flanged Groove Apertures

In the context of grating couplers, how the presence of iris-type slits across the groove apertures created by metallic strips lined over the ridge-bars of the gratings may influence the modal slab power and its bandwidth is also now investigated. As seen from Fig. 7, which presents the same kind of contour patterns as before in the preceding figure but just this time with $a_{\ell o}/g = a_{up}/g$ constituting the variable along the vertical axis, i.e., same iris-type slit-width on both sides. It is clearly demonstrated how the value of around 0.6 for this parametric ratio can broaden the slab-power bandwidth.

Such contour plots thus serve as important design charts for tailoring to whatever specifications that are desired by the application.

2.2. Grating Pulse Compression or Decompression

Grating pulse compressors or stretchers [8–13] constitute an integral part of chirped pulse amplification (CPA). Among the goals of these technologies include producing efficient energy extraction for high-power laser applications, particle acceleration [12], and material dispersion compensation [17, 18].

The mechanism of pair-grating pulse compression and decompression is now briefly described. Consider in Fig. 8 the schematic and its associated Floquet diagram entailing just the k_x axis along

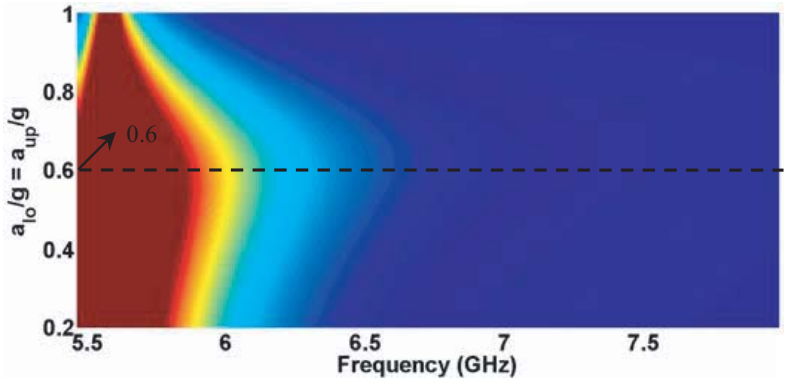

Figure 7. Contour plot of normalized power carried by $m = +1$ Floquet harmonic fast-space wave of bounded slab-mode within dielectric layer just above gratings against frequency and $a_{\ell o}/g = a_{up}/g$ for (a) TM^z polarized incidence with $\phi_{inc} = 0$ and $\theta_{inc} = 30°$, with $d_x = 20\,\text{mm}$, $\varepsilon_{grv}/\varepsilon_0 = 1.0$, $h = 12\,\text{mm}$, $g = 14\,\text{mm}$, $\varepsilon_{\ell o}/\varepsilon_0 = 1$, $\varepsilon_{up}/\varepsilon_0 = 10.2$, $d_{up} = 1.27\,\text{mm}$.

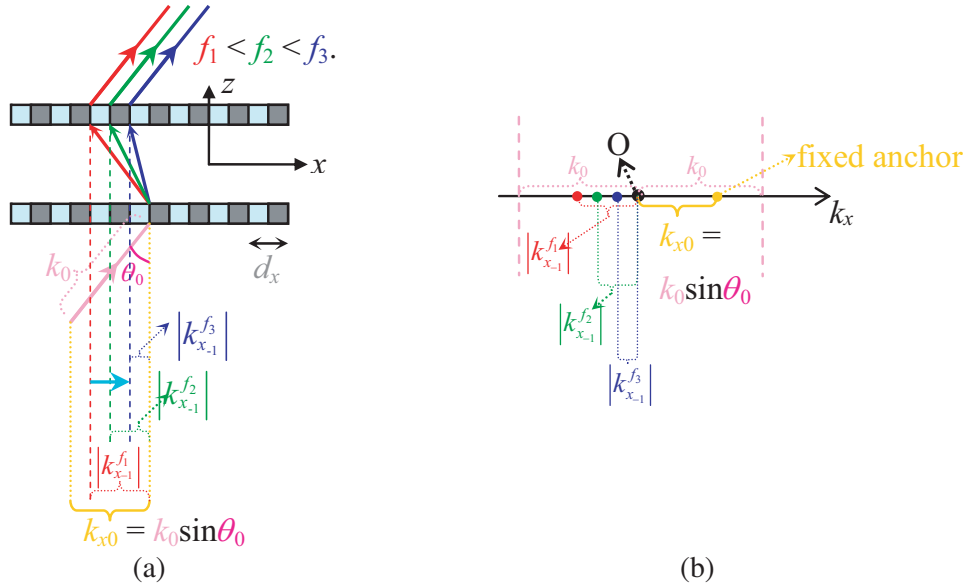

Figure 8. Mechanism of pair-grating pulse compression/decompression: (a) schematic and ray diagram, and (b) associated Floquet lattice diagram. In (a), the period d_x is fixed and the sole horizontal arrow depicts the reduction of $|k_{x-1}|$ with rising frequency associated with *squeezed Floquet nodal lattice*. In (b), the two vertical dashed lines define the fixed peripheries of real space for all frequencies. The anchor node of the dominant Floquet harmonic is as shown and those of the higher diffraction order of -1 at various frequencies shift rightwards as frequency increases. The difference in abscissa value between the fixed anchor and any of the -1 nodes is $2\pi/d_x$, which gets geometrically smaller in the lattice diagram (but not in its value, which is fixed) as frequency rises. For a fixed θ_0 in both (a) and (b), the $\sin\theta_0$ is correspondingly a constant.

which the lattice of discrete spectral nodes is aligned. For constant θ_0 and d_x, then with fixed peripheries of real space in the spectral diagram (drawn as two vertical dashed lines) with resultant anchored node of the dominant k_{x0} (due to a fixed $k_{x0}/k_0 = \sin\theta_0$), as the frequency increases along with an associated rise in k_0, the *amount of wavenumber per geometrical length* along the horizontal k_x axis also rises. Thus, the numerically-fixed inter-nodal separation, $2\pi/d_x$, must become *geometrically* smaller in the Floquet diagram, leading to lattice nodes that get closer (squeezed) together, all with respect to the anchored nodal point of the dominant k_{x0}. Note that the plane of incidence is the xz plane with $\phi_{inc} = 0$.

With this description, how the pair of gratings disperses the spectrum and stretches the input pulse is thus evident, whereby the angular spread of the incident wave into its various frequency components has been explained. An ultrashort laser pulse incident onto the grating-pair from its bottom as indicated by the ray arrow in Fig. 8 is stretched out in time prior to amplification. After penetrating the grating-pair, the chirped pulse, the intensity of which being much lower than that of its original ray, may then be safely introduced to the gain medium and amplified by factors that can reach the orders of over a million. The intensified waves are then recompressed back to their original pulse width through the reversed process entailing again a pair of gratings. Peak powers that are orders of magnitude greater than those of laser systems prior to the invention of CPA may hence be attained.

2.2.1. Bandwidth Enhancement of $m = -1$ Diffraction Order

As elucidated in the foregoing description, the role which the spectral range plays in determining the angular spread of the signal rays for pulse compression or stretching then motivates a need for maintained high transmission of the $m = -1$ Floquet harmonic for as wide a band of frequencies as possible. For brevity, just one maneuver for widening the bandwidth of this diffraction order is investigated, and that is to employ metallic fins across either side of each groove aperture to create iris-type slits.

For TM^z polarized incidence with $\phi_{inc} = 0$ and $\theta_{inc} = 30°$, Fig. 9 presents the contour plots of the transmission coefficient for the $m = -1$ Floquet harmonic against a_{up}/g and frequency, with $d_x = 20\,\text{mm}$, $g = a_{\ell o} = 14\,\text{mm}$, $\varepsilon_{grv}/\varepsilon_0 = 1$ (unfilled grooves), $h = 12\,\text{mm}$, and $\varepsilon_{up}/\varepsilon_0 = \varepsilon_{\ell o}/\varepsilon_0 = 1$ (uncovered on both sides), and for PEC gratings. The bandwidth can evidently be increased by creating iris-type slits across the output groove aperture using metal fins. For the present computed case, the largest bandwidth expansion without compromising transmission level is achieved with $a_{up}/g \approx 0.83$.

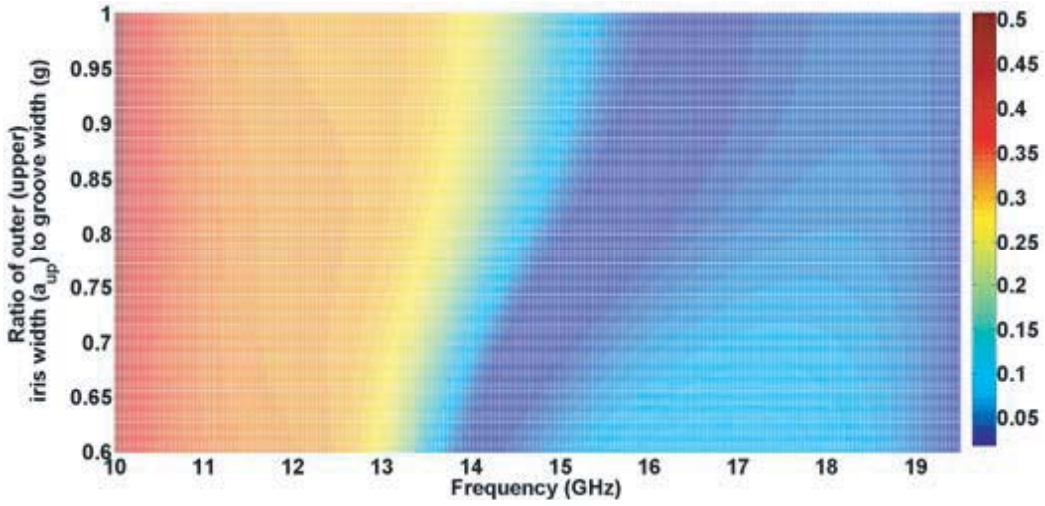

Figure 9. Contour plot of transmission coefficient for $m = -1$ diffraction order against a_{up}/g and frequency, for TM^z polarized incidence with $\phi_{inc} = 0$, $\theta_{inc} = 30°$, $d_x = 20\,\text{mm}$, $g = a_{\ell o} = 14\,\text{mm}$, $\varepsilon_{grv}/\varepsilon_0 = 1$, $h = 12\,\text{mm}$, $\varepsilon_{up}/\varepsilon_0 = \varepsilon_{\ell o}/\varepsilon_0 = 1$.

2.2.2. Scan-Width Enhancement of $m = -1$ Diffraction Order

As the incidence angle θ_{inc} varies, the beam direction of the $m = -1$ Floquet mode, as given by θ_{-1}^{diff} of (47) in [1], also changes (steered). Not only is this feature directly instrumental to beam deflectors in obvious ways, it also affords the less apparent option of controlling the degree of pulse compression or stretching, whereby smaller θ_{inc} gives rise to a wider spread of pulse stretching by transmission gratings and vice-versa. For this matter, it is thus important to gain insights into how the transmissivity of this $m = -1$ diffraction order is affected by the incidence angle and the ways through which the former

can be maintained high over as wide a span of the latter so as to offer broad tailorable ranges of pulse compression or stretching.

Just one maneuver shall be investigated for increasing the scan width of the $m = -1$ diffraction order, defined as the angular span over which the transmission of that higher-order Floquet harmonic is maintained at high levels, and that is the use of a dielectric slab cover placed on the input side.

With the input (lower) side of the gratings loaded with a dielectric layer, the contour plot of the transmission coefficient for the $m = -1$ mode against the input slab relative permittivity $\varepsilon_{\ell o}/\varepsilon_0$ and the incidence angle θ_{inc} at 14.8616 GHz is given in Fig. 10 for TM^z polarization with $\phi_{inc} = 0$, with $d_x = 20\,\text{mm}$, $g = a_{\ell o} = a_{up} = 14\,\text{mm}$ (no fins), $\varepsilon_{grv}/\varepsilon_0 = 1.0$ (unfilled grooves), $h = 12\,\text{mm}$, $\varepsilon_{up}/\varepsilon_0 = 1$, and $d_{\ell o} = 1.27\,\text{mm}$. As indicated by the horizontal dashed line in this figure that passes through the longest uninterrupted stretch of high transmissivity, it is evident that the scan-width may be optimally expanded by assigning to that input dielectric layer (of thickness 1.27 mm) a relative permittivity of around $\varepsilon_{up}/\varepsilon_0 = 17$. This is as opposed to not having any input sheath at all, as seen by the lower boundary of the contour plot representing $\varepsilon_{\ell o}/\varepsilon_0 = 1$.

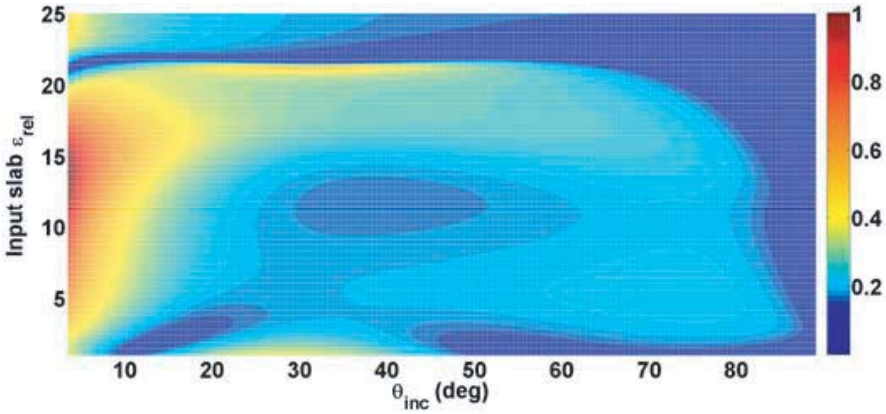

Figure 10. Contour plot of transmission coefficient for $m = -1$ diffraction order against *input* slab relative permittivity $\varepsilon_{\ell o}/\varepsilon_0$ and θ_{inc}, at 14.8616 GHz for TM^z polarized incidence with $\phi_{inc} = 0$, $d_x = 20\,\text{mm}$, $g = a_{\ell o} = a_{up} = 14\,\text{mm}$ (no fins), $\varepsilon_{grv}/\varepsilon_0 = 1.0$, $h = 12\,\text{mm}$, $\varepsilon_{up}/\varepsilon_0 = 1$, $d_{\ell o} = 1.27\,\text{mm}$.

2.3. Resolution of Gratings for Spectroscopy

In spectroscopy, the resolution of a grating is an important parameter as it quantifies its ability to tell apart between adjacent spectral lines. The limit of resolution is the minimum difference in frequency between two lines of equal intensity that can be distinguished, which by the Rayleigh criterion, gives the smallest separation between two neighboring frequencies whose intensity maxima are resolvable, i.e., identifiable as distinct spectral lines, any step less than which would result in ambiguity.

Consider a fixed incidence angle ($0 < \theta_{inc} = \theta_0 < \pi/2$, $0 < \phi_{inc} = \phi_0 < \pi/2$) (pertaining to the $m = 0$ dominant Floquet mode) and a prescribed diffraction angle ($0 < \theta^{diff} < \pi/2$, $\pi/2 < \phi^{diff} < \pi$) of the $m < 0$ harmonic, where θ^{diff} is the zenith angle measured from the vertical z axis perpendicular to the gratings while ϕ^{diff} is the usual azimuth angle measured from the x towards the y axis. The following general relation then applies [1]:

$$\sin\theta^{diff}\cos\varphi^{diff} - \sin\theta_0\cos\varphi_0 = -\lambda_0^{\Delta}/d_x \tag{2}$$

where $\lambda_0^{\Delta} = [f^{\Delta}\sqrt{(\mu_0\varepsilon_0)}]^{-1}$ is the free-space wavelength at the frequency f^{Δ} constituting the basic unit step such that at other higher frequencies of $f^{\#\kappa} = \kappa f^{\Delta}$ (κ being a positive integer), the diffraction order $m = -\kappa$ is radiated towards that same fixed direction of ($0 < \theta^{diff} < \pi/2$, $\pi/2 < \phi^{diff} < \pi$).

Clearly then, the smaller this inter-order separation f^{Δ} is (or the larger λ_0^{Δ} is), the higher will be the resolution. By this latter statement of the direct correlation between the resolution and λ_0^{Δ}, it can be asserted that, for a given gratings period d_x, the resolution increases with the magnitude of the

negative quantity ($\sin\theta^{diff}\cos\phi^{diff} - \sin\theta_0\cos\phi_0$) of the left-hand side (LHS) of Eq. (2). Subsequently, it is evident that a maximal λ_0^{Δ} arises when ($\theta^{diff} = 90°$, $\phi^{diff} = 180°$) and ($\theta_0 = 90°$, $\phi_0 = 0$) resulting in a maximally negative value of -2 on the LHS of Eq. (2), with associated $d_x = \lambda_0^{\Delta}/2$ under this condition of maximum resolution. If, however, $\phi_0 = 90°$ (yz plane of incidence parallel with gratings) resulting in a vanishing subtracted quantity $\sin\theta_0\cos\phi_0$, this does not affect the diffraction angle ($0 < \theta^{diff} < \pi/2$, $\pi/2 < \phi^{diff} < \pi$), which remains user-prescribed and highest resolution is still obtained by maximizing the negativity of the solely remaining negative quantity: $\sin\theta^{diff}\cos\phi^{diff}$ (again attained by $\theta^{diff} = \pi/2$, $\phi^{diff} = \pi$).

We shall now explore the prospects of tailoring any of the various parameters of the present generally dielectric slab covered penetrable gratings with optional strip-loaded bars to enhance the transmission into every one of the various diffraction orders $m = -\kappa$ at each of the different frequencies $f^{\#\kappa} = \kappa f^{\Delta}$ for prescribed high levels of resolution of the gratings. Herein investigated is the use of dielectric cover sheets clad over the output side of the gratings to maintain high transmission levels of the various diffracted orders throughout the investigated spectrum configured for high resolution.

2.3.1. Permittivity of Dielectric Slab Cover on Output Side

Starting with studying the permittivity of this dielectric slab lined over the output side, consider another case of high resolution with large values of $\theta^{diff} = 85°$ and $\theta_0 = \theta_{inc} = 80°$, along with $\phi^{diff} = 180°$ and $\phi_0 = \phi_{inc} = 0$. Fig. 11 exhibits the contour plot of the transmission coefficients of various $m = -\kappa$ Floquet harmonic fast-space waves, all radiated towards that prescribed direction of diffraction defined by $\theta^{diff} = 85°$ in real space on the output side above the gratings against the relative permittivity, $\varepsilon_{up}/\varepsilon_0$, of that output slab cover and discrete frequency points $f^{\#\kappa} = \kappa f^{\Delta}$ (50 of them, i.e., $\kappa = 1$ to 50, with $f^{\Delta} = 15.133\,\text{GHz}$) for TM^z polarized incidence with $\phi_0 = \phi_{inc} = 0$ and $\theta_{inc} = 80°$, for $d_x = 10\,\text{mm}$, $g = a_{\ell o} = a_{up} = 9.6\,\text{mm}$ (no fins), $\varepsilon_{grv}/\varepsilon_0 = 2$, $h = 8\,\text{mm}$, $\varepsilon_{\ell o}/\varepsilon_0 = 1$, $d_{up} = 5\,\text{mm}$ (covered only on the output upper side). Numerous thin stretches of bright regions are observed in this plot. Evidently, the widest frequency span over which the transmission strength is preserved without interruption is achieved by about $\varepsilon_{up}/\varepsilon_0 = 4.9$ corresponding to the only elongated stretch among all bright strokes that is essentially horizontal (as annotated in the plot), demonstrative of continuously maintained transmission levels. It is worth stressing that this horizontal stretch of high transmission is the solitary one that is observable in the investigated parametric space. Hence, this optimal condition is nowhere abundant.

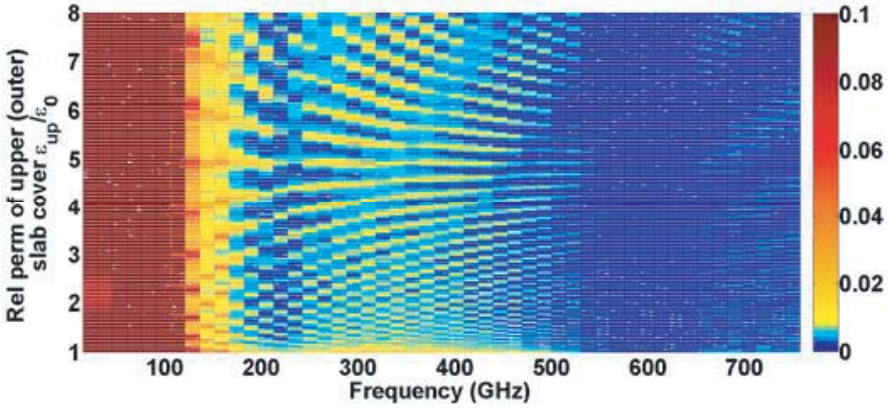

Figure 11. Contour plot of transmission coefficient of various $m = -\kappa$ Floquet harmonic fast-space waves all radiated towards universally fixed angular direction of diffraction $\theta^{diff} = 85°$ in real space on output side above gratings against upper (outer) slab cover relative permittivity $\varepsilon_{up}/\varepsilon_0$ and discrete frequency points $f^{\#\kappa} = \kappa f^{\Delta}$ (50 of them, i.e., $\kappa = 1$ to 50, with $f^{\Delta} = 15.133\,\text{GHz}$) for TM^z polarized incidence with $\phi_{inc} = 0$ and $\theta_{inc} = 80°$, for $d_x = 10\,\text{mm}$, $g = a_{\ell o} = a_{up} = 9.6\,\text{mm}$ (no fins), $\varepsilon_{grv}/\varepsilon_0 = 2$, $h = 8\,\text{mm}$, $\varepsilon_{\ell o}/\varepsilon_0 = 1$, $d_{up} = 5\,\text{mm}$ (slab-covered only on upper output side). Optimal $\varepsilon_{up}/\varepsilon_0$ of about 4.9 with the longest horizontal stretch of continuously maintained transmission levels.

2.3.2. Thickness of Dielectric Slab Cover on Output Side

Proceeding with inspecting how the thickness d_{up} of the sheath layer may enhance the performance of high-resolution gratings, consider now yet one more different case of large values of $\theta^{diff} = 75^\circ$ and $\theta_0 = \theta_{inc} = 80^\circ$, accompanied again by $\phi^{diff} = 180^\circ$ and $\phi_0 = \phi_{inc} = 0$. This adopts the case of [1], as do the upcoming materials. Fig. 12 then conveys the contour plot of the transmission coefficient of various $m = -\kappa$ Floquet harmonic fast-space waves all radiated towards the designated diffraction direction defined by $\theta^{diff} = 75^\circ$ in real space on the output side above the gratings against the upper (outer) slab cover thickness d_{up} and discrete frequency points $f^{\#\kappa} = \kappa f^{\Delta}$ (50 of them, i.e., $\kappa = 1$ to 50, with $f^{\Delta} = 15.3682\,\text{GHz}$) for TM^z polarized incidence with $\phi_{inc} = 0$ and $\theta_{inc} = 80^\circ$, for $d_x = 10\,\text{mm}$, $g = a_{\ell o} = a_{up} = 9.6\,\text{mm}$ (no fins), $\varepsilon_{grv}/\varepsilon_0 = 2$, $h = 8\,\text{mm}$, $\varepsilon_{\ell o}/\varepsilon_0 = 1$, and $\varepsilon_{up}/\varepsilon_0 = 3$ (slab-covered only on the upper output side). Numerous thin stretches of bright elongated horizontal regions are again observed. Further inspection reveals that the most horizontal one is associated with $d_{up} = 6.8\,\text{mm}$, as annotated in the plot. As before, this horizontal stretch of strong transmission is the only one that can be found from the considered parametric space, thus indicating the scarcity of this optimum situation.

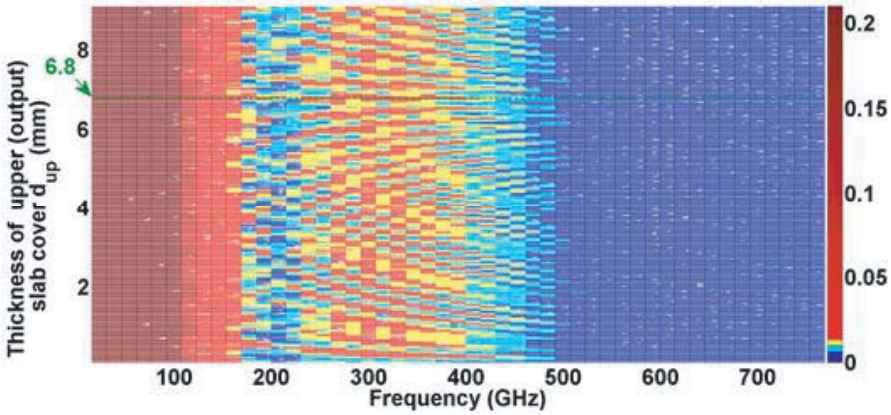

Figure 12. Contour plot of transmission coefficient of various $m = -\kappa$ Floquet harmonic fast-space waves all radiated towards universally fixed angular direction of diffraction $\theta^{diff} = 75^\circ$ in real space on output side above gratings against upper (outer) slab cover thickness d_{up} and discrete frequency points $f^{\#\kappa} = \kappa f^{\Delta}$ (50 of them, i.e., $\kappa = 1$ to 50, with $f^{\Delta} = 15.3682\,\text{GHz}$) for TM^z polarized incidence with $\phi_{inc} = 0$ and $\theta_{inc} = 80^\circ$, for $d_x = 10\,\text{mm}$, $g = a_{\ell o} = a_{up} = 9.6\,\text{mm}$ (no fins), $\varepsilon_{grv}/\varepsilon_0 = 2$, $h = 8\,\text{mm}$, $\varepsilon_{\ell o}/\varepsilon_0 = 1$, $\varepsilon_{up}/\varepsilon_0 = 3$ (slab-covered only on upper output side). Optimal $d_{up} = 6.8\,\text{mm}$ with longest horizontal stretch of continuously maintained transmission levels; after [1].

3. EXPERIMENTATIONS ON FABRICATED PROTOTYPE

A prototype of the diffraction gratings made of aluminum was manufactured in the form of a square frame with total dimensions of 500 mm by 500 mm. The parameters of this fabricated structure are as follow: cell size $d_x = 20\,\text{mm}$, groove width $g = a_{up} = a_{\ell o} = 14\,\text{mm}$ (no fins to create iris slits), depth $h = 12\,\text{mm}$, $\varepsilon_{grv} = \varepsilon_0$ (unfilled grooves), and $\varepsilon_{up} = \varepsilon_{\ell o} = \varepsilon_0$ (uncovered on both sides).

The experimental outcomes of two Floquet modal harmonics shall be reported: the dominant $m = 0$ mode, and the most common next higher diffraction order of $m = -1$, each of which as presented in the upcoming subsections.

3.1. Transmission and Reflection for $m = 0$ Floquet Harmonic

The measured transmission and reflection of the dominant $m = 0$ Floquet mode of the manufactured grating are herein presented. Alongside a schematic of the experimental setup in Fig. 13(a) is the corresponding photograph of this grating placed under its measurement scenario in Fig. 13(b). The

saw-tooth portions in the former represent absorbers. Two horns are connected to both ports of the Anritsu MS4644B vector network analyzer, one serving as the transmitter and the other as the receiver. By adjusting the directions of the gratings relative to the horns, the S_{11} and S_{21} may be measured for various scenarios of polarizations and incidence angles. Doing so for TM^z polarization with $\phi_{inc} = 90°$ and $\theta_{inc} = 0$, the measured reflection and transmission coefficients over a range from 8 to 18 GHz are presented in Figs. 14(a) and 14(b) respectively, each being compared with its theoretical prediction computed by the code based on the present formulation. As seen, good agreement is achieved.

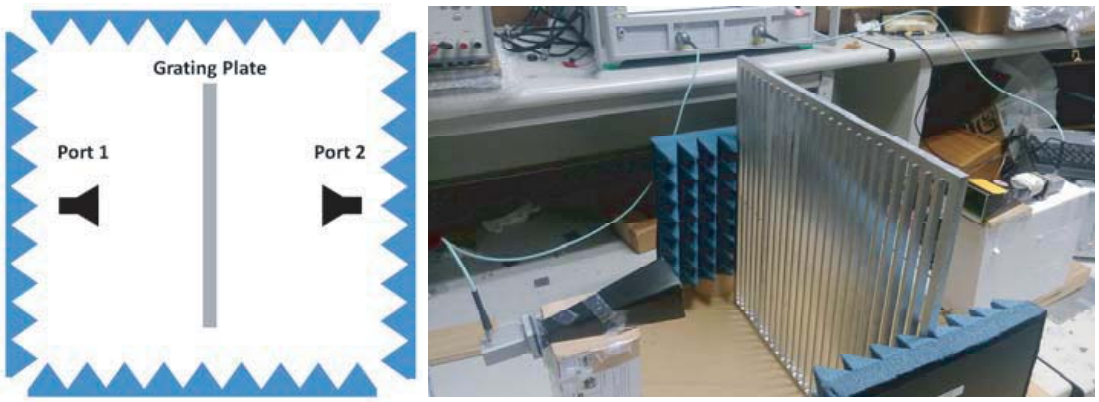

(a) (b)

Figure 13. Measurement of reflection and transmission for $m = 0$ Floquet mode using a vector network analyzer; (a) schematic of the experimental setup, and (b) photograph of the manufactured grating and the two horns under the measurement scenario.

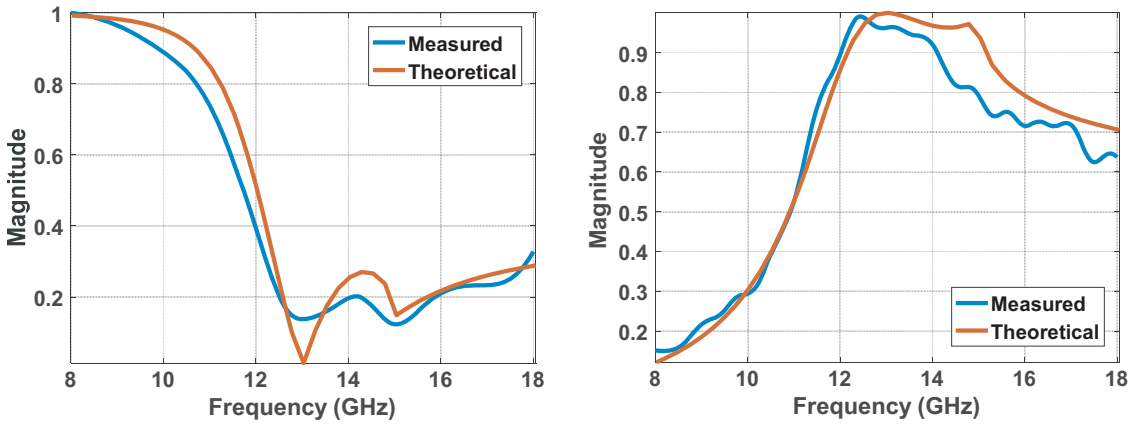

(a) (b)

Figure 14. Variation with frequency of measured (a) reflection and (b) transmission coefficients of $m = 0$ dominant Floquet harmonic for TM^z polarization with $\phi_{inc} = 90°$, $\theta_{inc} = 0$, held up against theoretical predictions obtained by present formulation.

3.2. Radiation into Transmitted $m = -1$ Diffraction Order

The measurement of the $m = -1$ diffraction mode was conducted in an anechoic chamber, whereby both the Ku-band horn feed and the gratings were mounted on top of the rotating platform as photographed in Fig. 15(b) and in which the receiving antenna at the further end also shows up. A schematic of the experimental scenario is given alongside in Fig. 15(a).

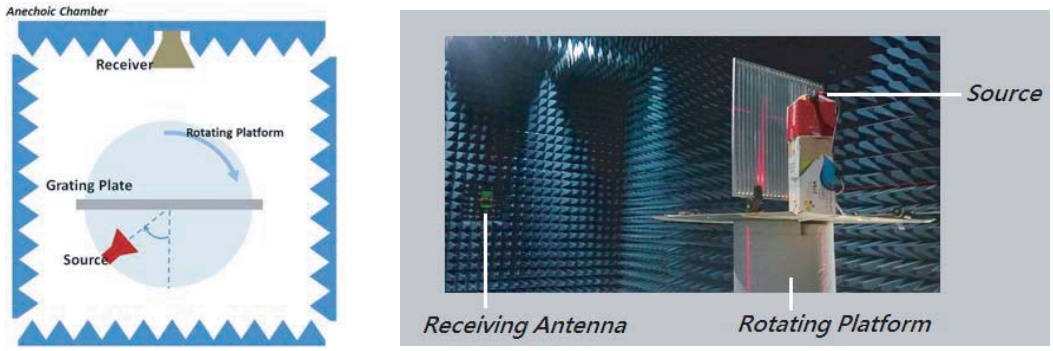

(a) (b)

Figure 15. Measurement of $m = -1$ diffraction order conducted in anechoic chamber: (a) schematic of experimental setup, and (b) photograph of measurement scenario in anechoic chamber.

By manually rotating the direction of the source along various incidence angles $\theta_0 = \theta_{inc}$ on the platform, the radiation levels towards the corresponding directions defined by $\theta^{diff}_{m=-1}$ according to (47) of the $m = -1$ diffraction order that is transmitted over to the output side of the gratings were measured. For TM^z polarization with $\phi_{inc} = 0$, the variations of this measured radiation magnitude with θ_{inc} at 14.86 GHz and with frequency for $\theta_{inc} = 30°$ are graphed respectively in Figs. 16(a) and 16(b), within each of which the corresponding theoretical trace is embedded. The experimental outcomes in both plots are seen to corroborate well with their respective predictions by theory.

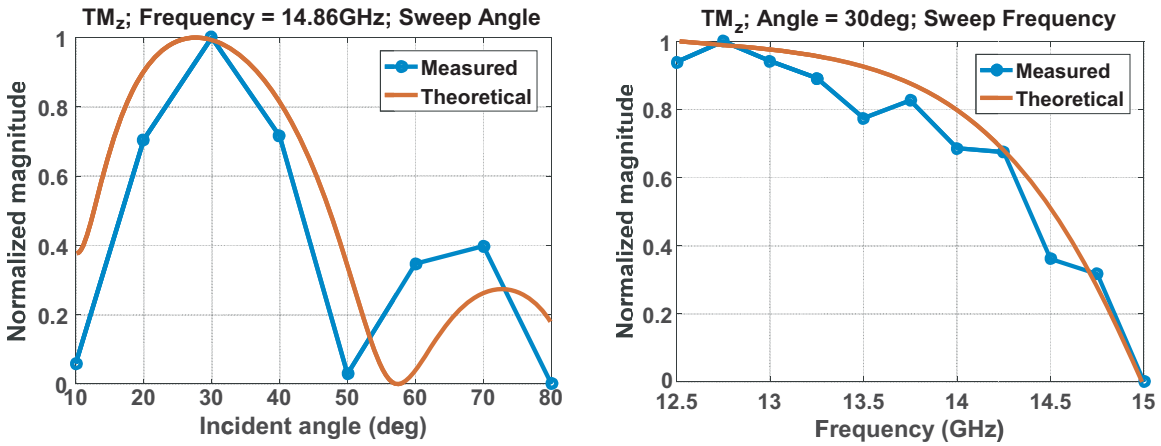

(a) (b)

Figure 16. Measured radiation of $m = -1$ transmitted diffraction order compared with theoretical expectation for TM^z polarization with $\phi_{inc} = 0$: (a) variation with θ_{inc} at 14.86 GHz, and (b) variation with frequency for $\theta_{inc} = 30°$.

3.3. Experimental Validation of Grating Couplers

This section seeks to experimentally validate the results of Fig. 5, which portrayed peaks of the $m = 1$ Floquet mode flowing within the dielectric slab of a grating coupler at specific combinations of frequencies and angles of incidence according to Eq. (1) and the dispersion diagram of Fig. 4, the grating of which has been manufactured. In the present measurement setup, an additional dielectric slab (Rogers RO4003C) with dielectric constant of 3.38 and thickness of 1.524 mm (parameters of Figs. 4 and 5) is now mounted right on the aluminum grating. As schematized and photographed in Figs. 17(a)

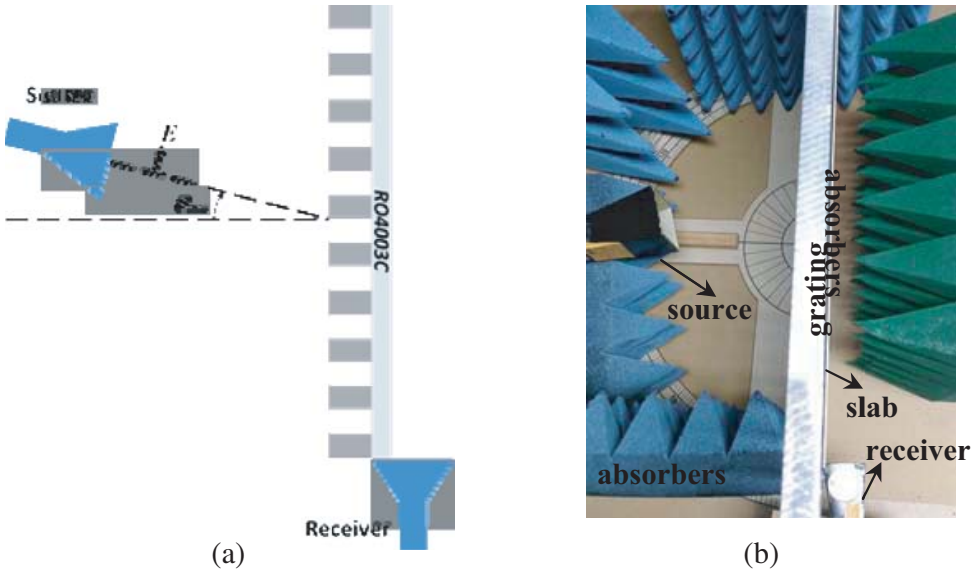

(a) (b)

Figure 17. Experimental setup for measuring $m = 1$ modal slab power of a grating coupler composed of the same manufactured grating as before and now with a dielectric sheet of $\varepsilon_{rel} = 3.38$ and thickness 1.524 mm (Rogers RO4003C) placed over the grating; (a) Schematic, and (b) Photograph of actual measurement setting for the case of $\theta_{inc} = -8.02°$.

and 17(b) respectively, a horn antenna source is oriented for the launching of TM^z polarized incident waves with $\phi_{inc} = 0$ as was in the theoretical study and a receiving horn antenna is aligned along the edge of the dielectric sheet of the grating coupler to measure the bounded slab modal wave. The entire setup is surrounded by absorbers to absorb the reflected and transmitted dominant $m = 0$ waves, thus retaining mainly the influence of the diffracted slab modal wave picked up by the receiver.

Figure 18 presents the variation with frequency of the measured normalized $m = 1$ slab modal received power of grating coupler, for $\theta_{inc} = -8.02°$ and $-0.7842°$ as annotated in the graph. Peaks occur at 13.3 GHz and 14.6 GHz respectively for these two incidence angles, which are indeed close to theoretical predictions of Fig. 5.

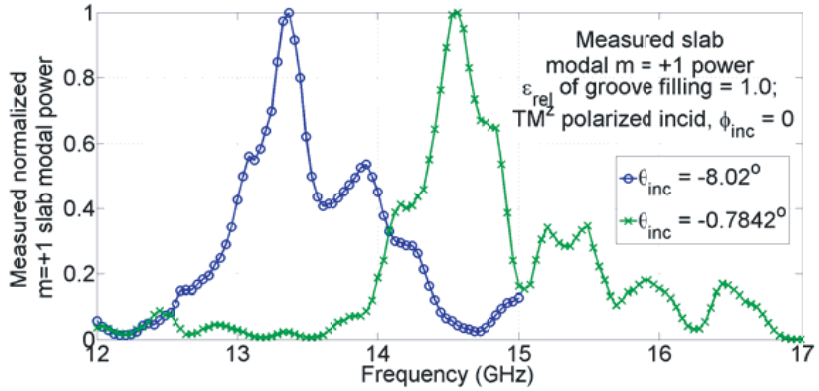

Figure 18. Measured normalized $m = +1$ slab modal power of grating coupler, for $\theta_{inc} = -8.02°$ and $-0.7842°$ as annotated. Peaks occur at 13.3 GHz and 14.6 GHz respectively, which are close to theoretical predictions of Fig. 12.

4. SENSITIVITY ANALYSES FOR TOLERANCE ERRORS IN THE MANUFACTURE OF PROTOTYPES

Due to tolerance errors in the fabrication of the prototypes, it would be relevant to investigate how the grating behavior fluctuates when physical parameters vary about their designated values. The typical dimensional tolerance of fabrication vendors with high-precision machinery is about $+/-0.1$ mm. A sensitivity analysis is thus presented herein for three geometrical properties, namely the period d_x,

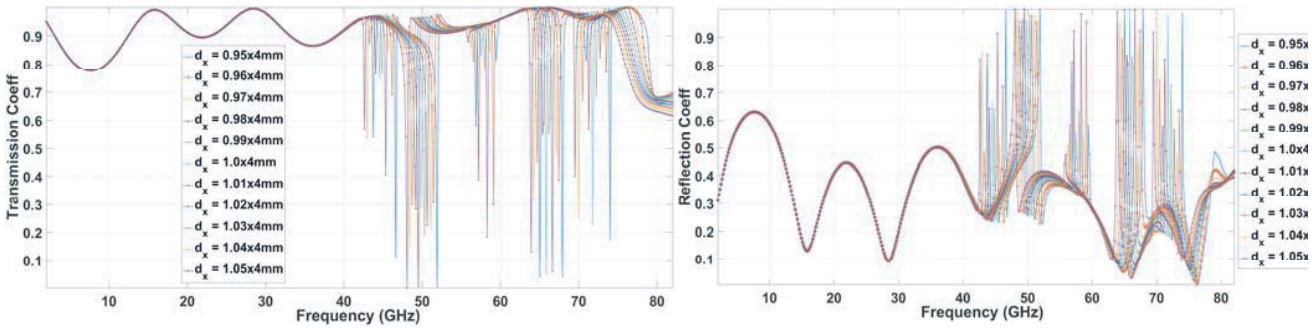

(a) (b)

Figure 19. (a) Transmission and (b) reflection spectra of the case of Fig. 5 of [1] for various tolerance errors in the period d_x about the desired value of 4 mm, as annotated.

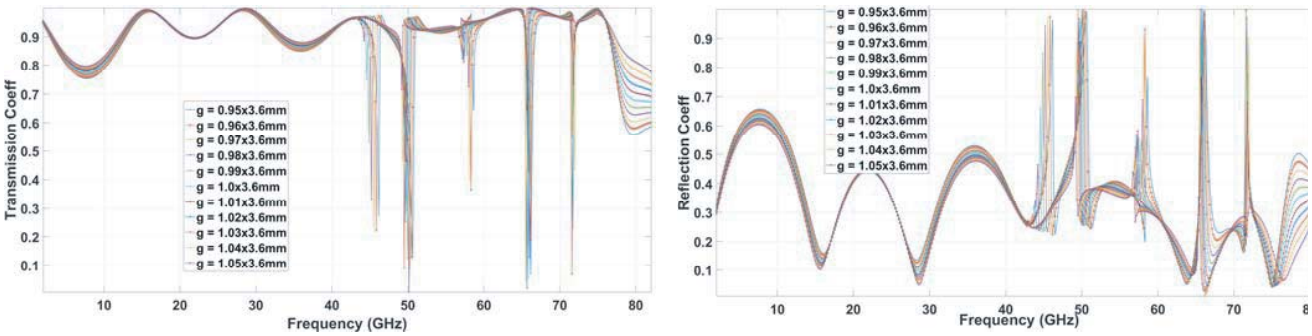

(a) (b)

Figure 20. (a) Transmission and (b) reflection spectra of the case of Fig. 5 of [1] for various tolerance errors in the groove width g about the desired value of 3.6 mm, as annotated.

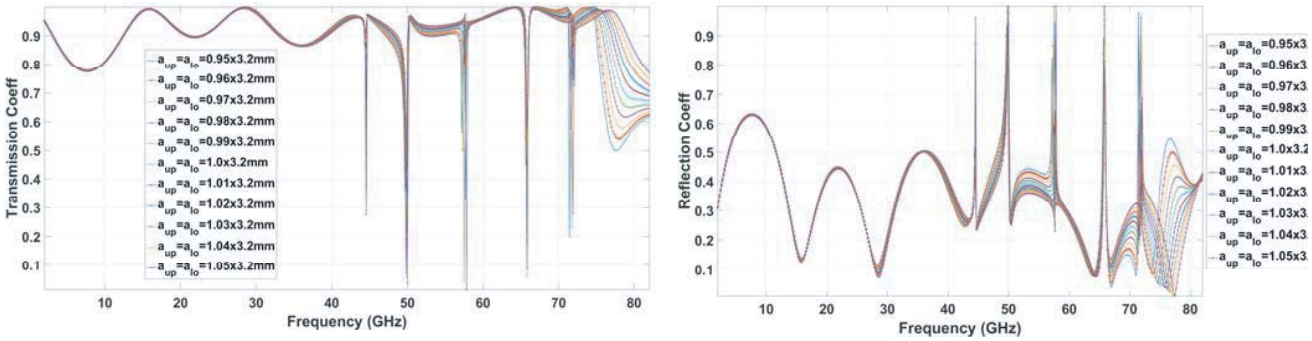

(a) (b)

Figure 21. (a) Transmission and (b) reflection spectra of the case of Fig. 5 of [1] for various tolerance errors in the aperture width $a_{up} = a_{\ell o}$ about the desired value of 3.2 mm, as annotated.

groove-width g, and the aperture width that is equal on both sides, i.e., $a_{up} = a_{\ell o}$. For the configuration of Fig. 5 in [1], Fig. 19 presents the transmission and reflection spectra computed by the code written based on the modal method of [1] for various levels of errors in the period about the intended value of 4 mm, as indicated in the legend. The corresponding graphs are conveyed in Figs. 20 and 21 for fluctuations in the groove and aperture widths about their desired values of 3.6 mm and 3.2 mm, all respectively. As can be seen, despite errors even as severe as 5%, being levels which are well within most manufacture tolerances, the spectral properties remain highly consistent, especially at frequencies not exceeding 40 GHz for the considered structure, which is already an extremely high maximum frequency. Hence, these results allay the concern about the risk of compromised accuracies in the measurement results due to errors within tolerable limits in fabrication processes.

5. CONCLUSIONS

Afforded by the analytical tool of a presented article is the ability to study higher-ordered diffraction modes other than the fundamental Floquet harmonic, particularly those of $m = -1$ and $+1$, which are typically the two most relevant ones in the context of numerous applications ranging from mode converters and beam deflectors to grating couplers, pulse compression gratings, and diffraction gratings in spectroscopy. The capabilities of these applications, such as the strengthening of transmission of the higher order Floquet harmonics, as well as the bandwidth and scan-width over which this is achieved, have all been demonstrated in this paper to be improvable by tailoring the new parameters of the special configuration.

A prototype of the grating was fabricated and measured. For both the fundamental $m = 0$ mode and often the most pertinent next higher diffraction order of $m = -1$, experimental results that agree well with results predicted by the analytical modal technique herein presented were successfully attained. The underlying mechanism of resonance coupling between a surface-wave mode and a higher order Floquet harmonic within the dielectric slab had also been experimentally verified by measurements conducted on a manufactured grating coupler.

This work has thus opened the doors to new horizons for exploring the prospects of employing dielectric slab covers on either or both sides of a diffraction grating, groove fillings, as well as iris-type slits across the groove apertures created by metallic fins loaded over the conducting bars to achieve better performances in numerous applications that utilize such grating structures.

ACKNOWLEDGMENT

This work was partially supported by the "Center for mmWave Smart Radar Systems and Technologies" under the Featured Areas Research Center Program within the framework of the Higher Education Sprout Project by the Ministry of Education (MOE) in Taiwan, and partially supported by the Ministry of Science and Technology (MOST) of Taiwan under Grant numbers MOST 109-2634-F-009-030 and 107 -2221 -E -009 -051-MY2.

REFERENCES

1. Ng Mou Kehn, M. and W. Y. Lai, "Modal analysis of gratings with conducting strip-loaded bars and sandwiched between multiple dielectric layers," *IEEE Trans. Antennas Propag.*, Vol. 68, No. 6, 5027–5032, Jun. 2020.
2. Tamir, T. and H. L. Bertoni, "Lateral displacement of optical beams at multilayered and periodic structures," *J. Opt. Soc. Amer.*, Vol. 61, 1397–1413, 1971.
3. Harris, J. H., R. K. Winn, and D. G. Dalgoutte, "Theory and design of periodic couplers," *Appl. Opt.*, Vol. 11, 2234–2241, 1972.
4. Peng, S. T., T. Tamir, and H. L. Bertoni, "Leaky wave analysis of optical periodic couplers," *Electron. Lett.*, Vol. 9, 150–152, 1973.
5. Kneubühl, F., "Diffraction grating spectroscopy," *Appl. Opt.*, Vol. 8, 505–519, 1969.

6. Kiang, M. H., J. T. Nee, K. Y. Lau, and R. S. Muller, "Surface-micromachined diffraction gratings for scanning spectroscopic applications," *Proceedings of International Solid State Sensors and Actuators Conference (Transducers '97)*, Vol. 1, 343–345, Chicago, IL, USA, 1997.
7. Ge, J., D. L. McDavitt, J. L. Bernecker, S. Miller, D. R. Ciarlo, and P. J. Kuzmenko, "Development of silicon grisms and immersion gratings for high-resolution infrared spectroscopy," *Proc. SPIE 4485, Optical Spectroscopic Techniques, Remote Sensing, and Instrumentation for Atmospheric and Space Research IV*, Jan. 30, 2002, https://doi.org/10.1117/12.454275.
8. Treacy, E. B., "Optical pulse compression with diffraction gratings," *IEEE J. Quantum Electron.*, Vol. 5, No. 9, 454–458, Sep. 1969.
9. Heritage, J. P., R. N. Thurston, W. J. Tomlinson, A. M. Weiner, and R. H. Stolen, 'Spectral windowing of frequency-modulated optical pulses in a grating compressor," *Appl. Phys. Lett.*, Vol. 47, No. 2, 87–89, Jul. 1985.
10. Martinez, O. E., "3000 times grating compressor with positive group velocity dispersion: application to fiber compensation in 1.3–1.6 μm region," *IEEE J. Quantum Electron.*, Vol. 23, No. 1, 59–64, Jan. 1987.
11. Gomes, A. S. L., A. S. Gouveia-Neto, and J. R. Taylor, "Optical fibre-grating pulse compressors," *Opt. & Quant. Electronics*, Vol. 20, 95–112, 1988.
12. Zhang, T., M. Yonemura, and Y. Kato, "An array-grating compressor for high-power chirped-pulse amplification lasers," *Opt. Commun.*, Vol. 145, 367–376, Jan. 1998.
13. Jia, W., C. Zhou, J. Feng, and E. Dai, "Miniature pulse compressor of deep-etched gratings," *Appl. Opt.*, Vol. 47, No. 32, 6058–6063, Nov. 2008.
14. Deguzman, P. C. and G. P. Nordin, "Stacked subwavelength gratings as circular polarization filters," *Appl. Opt.*, Vol. 40, 5731–5737, 2001.
15. Bird, G. R. and M. Parrish, "The wire grid as a near-infrared polarizer," *J. Opt. Soc. Am.*, Vol. 50, 886–891, 1960.
16. Weber, T., S. Kroker, T. Käsebier, E.-B. Kley, and A. Tünnermann, "Silicon wire grid polarizer for ultraviolet applications," *Appl. Opt.*, Vol. 53, 8140–8144, 2014.
17. Kane, S. and J. Squier, "Grating compensation of third-order material dispersion in the normal dispersion regime: Sub-100-fs chirped-pulse amplification using a fiber stretcher and grating-pair compressor," *IEEE J. Quantum Electron.*, Vol. 31, No. 11, 2052–2057, Nov. 1995.
18. Gibson, E. A., D. M. Gaudiosi, H. C. Kapteyn, and R. Jimenez, "Efficient reflection grisms for pulse compression and dispersion compensation of femtosecond pulses," *Opt. Lett.*, Vol. 31, No. 22, 3363–3365, Nov. 2006.